Lattice-Matched Epitaxial Graphene Grown on Boron Nitride
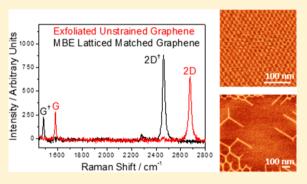
Andrew Davies,[†,‡] Juan D. Albar,[†] Alex Summerfield,[†] James C. Thomas,[†] Tin S. Cheng,[†] Vladimir V. Korolkov,[†] Emily Stapleton,[†] James Wrigley,[†] Nathan L. Goodey,[†] Christopher J. Mellor,[†] Andrei N. Khlobystov,[‡] Kenji Watanabe,[§] Takashi Taniguchi,[§] C. Thomas Foxon,[†] Laurence Eaves,[†] Sergei V. Novikov,[†] and Peter H. Beton*,[†]

[†]School of Physics and Astronomy, University of Nottingham, Nottingham NG7 2RD, United Kingdom
[‡]School of Chemistry, University of Nottingham, Nottingham NG7 2RD, United Kingdom
[§]National Institute for Materials Science, 1-1 Namiki, Tsukuba, Ibaraki 305-0044, Japan

S *Supporting Information*

ABSTRACT: Lattice-matched graphene on hexagonal boron nitride is expected to lead to the formation of a band gap but requires the formation of highly strained material and has not hitherto been realized. We demonstrate that aligned, lattice-matched graphene can be grown by molecular beam epitaxy using substrate temperatures in the range 1600−1710 °C and coexists with a topologically modified moiré pattern with regions of strained graphene which have giant moiré periods up to ∼80 nm. Raman spectra reveal narrow red-shifted peaks due to isotropic strain, while the giant moiré patterns result in complex splitting of Raman peaks due to strain variations across the moiré unit cell. The lattice-matched graphene has a lower conductance than both the Frenkel−Kontorova-type domain walls and also the topological defects where they terminate. We relate these results to theoretical models of band gap formation in graphene/boron nitride heterostructures.

KEYWORDS: *Graphene, boron nitride, growth, strain, band gap, epitaxy*

The fabrication of heterostructures formed by placing monolayer graphene on hexagonal boron nitride[1−3] (hBN) has provided a route to a diverse range of new phenomena including cloning of Dirac points, a commensurate−incommensurate transition and resonant tunnelling between chiral states.[4−9] The interest in hBN was originally motivated by its suitability as an ultraflat substrate with isostructural properties, and a close match in lattice parameters to graphene.[1,10,11] In fact, the mismatch between the lattice constants of hBN, a_{hBN}, and graphene, a_G, although small (∼1.8%), can strongly modify the electronic properties of graphene through the formation of a moiré pattern and an associated superlattice potential which modifies the electronic band structure, and leads to the formation of satellite Dirac points.[4,5,8] In addition, the symmetry between the A and B graphene sublattices is broken locally and, depending on whether there is a cancellation of this effect across the unit cell, can give rise to an energy gap at the Dirac point.[4,12−18] A more robust route to forming an energy gap has been predicted for G/hBN heterostructures in which the layers are lattice-matched;[14] in that case, the A/B sublattice symmetry is broken globally rather than locally. However, this would require a relative strain of ∼1.8% between the two materials which has not been realized to date and is widely considered to be unachievable. Here we demonstrate that lattice-matched graphene can be grown on hBN using molecular beam epitaxy

(MBE) and a substrate temperature, T_S, up to 1710 °C. The lattice-matched graphene is formed over areas of ∼1 μm^2 and results in a narrowing and shifting of the major peaks in the Raman spectrum. We also observe topologically modified moiré patterns in which dislocations act as sources for Frenkel−Kontorova-like domain walls and provide a mechanism for strain relief within the graphene monolayer. A spatial variation of the electrical conductance at room temperature, which we argue is consistent with the formation of a small energy gap, is also observed.

We have recently shown[19] that strained graphene can be grown on hBN using MBE and that it exhibits complex moiré patterns which can be highly anisotropic and have a period, λ_S, which is much greater than λ_0, the value (13.9 nm) expected for perfectly aligned unstrained graphene on hBN. The strained graphene has a lattice constant which is increased from the unstrained value, a_G, to $a_G + \Delta a_G$. This results in a reduction of the mismatch between the graphene and hBN lattice constants and, thus, a moiré pattern which has a longer period since $\lambda_S \approx a_G^2/(a_{hBN} − a_G − \Delta a_G)$, which would be expected to diverge for lattice-matched material. For samples grown at $T_S = 1500$

°C, higher than the growth temperatures typically used for epitaxial growth of graphene on hBN,[20−28] we have previously reported moiré periods up to ~30 nm, corresponding to a strain, $\Delta a_G/a_G \sim 0.9\%$. Note that here Δa_G is the deviation of the lattice constant averaged over the moiré period; Woods et al.[6] have proposed that a commensurate−incommensurate transition occurs in aligned G/hBN heterostructures leading to a small variation of the graphene lattice constant across the unit cell and this variation has recently been observed directly.[29]

We now demonstrate that the maximum strain present in our epitaxial material increases for growth temperatures above 1500 °C up to a condition where lattice-matching with hBN occurs. Figure 1 shows Raman spectra and images acquired by atomic
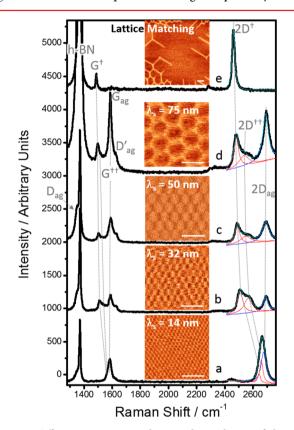

Figure 1. Offset Raman spectra showing the evolution of the red-shifting G and 2D bands with increasing moiré periodicity. The black lines are experimental data and the overlaid light blue lines are multi-Lorentzian fits to the 2D region; (a−d) have two red-shifted components, 2D†, 2D†† (the red curves), and a third unshifted band (dark blue) arising from carbon aggregates while (e) has a single red-shifted band. In the G region, there are two red-shifted peaks G†, G†† (one in (e)) together with the unshifted G_{ag} and D'_{ag} peaks arising from carbon aggregates ((b−e) only). Inset figures show AFM images recorded in AC mode in the vicinity of the location where the Raman spectrum was obtained (c is a phase image; a,b,d,e, are topographies). AFM scale bars are 100 nm; the moiré period λ_S ranges from 14 nm for unstrained graphene on hBN in (a) up to 75 nm in (d) and effectively diverges in (e) where the defect lines are topologically modified. Positions and widths of all peaks are tabulated in SI.

force microscopy (AFM; all images acquired at room temperature under ambient conditions) for regions of graphene grown by MBE on hBN for values of T_S ranging from 1550 °C up to 1710 °C. The hBN flakes used as substrates are exfoliated and mounted on a sapphire wafer. The substrate preparation, MBE growth system and other relevant growth parameters have

been described in our earlier work[30,31] and other relevant parameters are included in the Supporting Information (SI).

The AFM images (see SI) in Figure 1a−d shows regions with progressively larger moiré periods arising from increasing strain. In some areas (Figure 1a), we find a period ~14 nm which is close to the value expected for unstrained, aligned graphene on hBN, but the period is much larger in many regions, for example λ_S = 32, 50, and 75 nm in Figure 1b−d; these values correspond, respectively, to strains of 1.0%, 1.3%, and 1.5%, much larger than previously reported.[19] Most interestingly, in Figure 1e we observe topological differences in the moiré pattern; the boundaries around the repeating hexagonal units are broken up and terminate at specific points on the sample surface. Consequently, the regions of graphene bounded by the bright topographic features are very large and the moiré period effectively diverges. As we argue below, the low contrast regions in this AFM image, which extend over ~1 μm, correspond to lattice-matched graphene on hBN while the bright lines correspond to Frenkel−Kontorova (F−K) domain walls where the mismatch strain is localized as discussed by Woods et al.;[6] these lines terminate on defects in the graphene lattice.

The Raman spectra in Figure 1 were acquired at the locations of the corresponding AFM images and, as expected,[32−34] show that the presence of strain leads to pronounced changes in the spectral features. In Figure 1a−d, there are three peaks in the 2D band of the Raman spectra, two of which (here referred to as 2D† and 2D††) are red-shifted relative to unstrained relaxed graphene. A third peak, $2D_{ag}$ is associated with the presence of turbostratic graphene aggregates which coexist with monolayer graphene in some regions of the surface[19] as discussed below. The two red-shifted peaks were previously assigned[19] to strained graphene on hBN, and the spectra in Figure 1 show clearly that the trend for increasing red shift of the 2D† and 2D†† bands with increased moiré period continues well beyond the reported limit of λ_S = 30 nm.

The Raman spectrum shown in Figure 1e is qualitatively different; here we find a highly red-shifted, mono-Lorentzian 2D† peak at 2460 cm^{-1}, and both the 2D†† and $2D_{ag}$ bands are absent. In addition, we observe a clear red-shifted G peak, referred to as G†, at 1488 cm^{-1}. Remarkably, the complex splitting and broadening which is present in Figure 1a−d evolves into Raman peaks in Figure 1e which are much narrower with full width at half maximum (FWHM) of 22 and 13 cm^{-1} (2D† and G†, respectively), close to the values observed for high quality exfoliated graphene.[34] While we analyze the Raman data in detail below, these general observations provide direct evidence that the local environment of carbon atoms is much more uniform in regions such as in Figure 1e. Note that a graphene sheet subjected to isotropic strain would be expected to exhibit Raman peaks which are shifted in energy but due to the absence of symmetry breaking would not undergo splitting.[32] Such spectra have been reported for a graphene membrane under hydrostatic pressure[35,36] and for a quoted strain of 1.8% are very similar to those observed in Figure 1e, although our measured values of FWHM are significantly narrower. We also note that the relative intensity $I(2D^\dagger)/I(G^\dagger) \approx 3.8$, close to the value observed for exfoliated monolayer graphene.[34]

There are several other peaks present in the Raman spectra in Figure 1; in all spectra we observe the hBN E_{2g} phonon mode,[37] at 1366 cm^{-1}. The spectra in Figure 1a−d show a G†† peak associated with strained graphene (present as a shoulder on the G† peak), and several other peaks associated with the
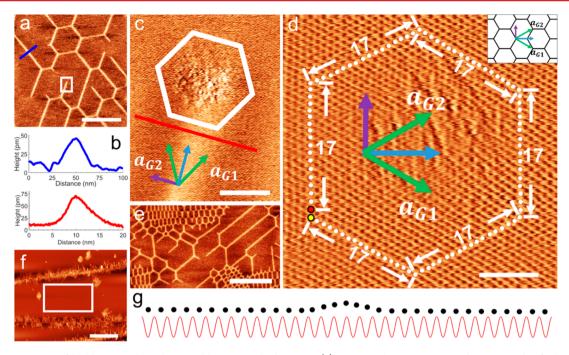
Figure 2. AFM images of highly strained graphene and lattice-matched regions. (a) Topographic image acquired in AC mode of a highly strained graphene region. High contrast lines correspond to Frenkel−Kontorova-like domain walls. Scale bar: 200 nm. (b) Height profile on path marked by blue line on (a) and along path marked in red in (c). (c) Contact mode topographic image of the area marked with the white rectangle in (a) showing the end of the defect line. The green, blue, and purple arrows indicate, respectively, the directions of the unit cell vectors, the defect line, and the measured Burgers vector corresponding to an edge dislocation. The white hexagon indicates the path used to obtain the Burgers vector. Scale bar: 5 nm. (d) Lattice resolution image (contact mode, deflection channel) of the end of the defect line. The image is 70° clockwise rotated with respect to (c). The dots with darker contrast are the gaps in the lattice, namely the centers of the graphene hexagons. Those centers colored in white indicate the Burgers path, which consists of steps over 17 lattice constants along each side of the hexagon, starting at the red dot and finishing at the yellow one. The fact that these two points are not coincident indicates that there is an enclosed dislocation. Inset on top-right shows a schematic of the graphene lattice. Scale bar: 2 nm. (e) Topographic AC mode image of an area similar to (a) on another hBN flake. Scale bar: 500 nm. (f) Topographic AC mode image of a larger area image showing the location of image (e) (marked by white rectangle) and neighboring carbon deposits. Scale bar: 1 μm. (g) Schematic vertical (and perpendicular to the ridge) cut of the graphene lattice (black dots) with the potential generated by the hBN lattice (red line). The graphene is strained and matches the hBN lattice on each side of the dislocation line.

presence of turbostratic graphene:[38,39] an unshifted G_{ag} peak (at ~1585 cm^{-1}); a D_{ag} shoulder on the hBN peak (at ~1350 cm^{-1}); and a D'_{ag} shoulder (at ~1625 cm^{-1}) on the unshifted G_{ag} peak. These peaks arise because the spot size of the Raman microscope (~1 μm^2) is larger than the typical separation of turbostratic graphene aggregates; see, for example, the large area images in Figure 2. At the higher growth temperatures, the density of aggregates is lower and we extract some spectra where the associated Raman peaks ($2D_{ag}$, G_{ag}, etc.) are completely absent (e.g., Figure 1e). Further discussion of these features and the fitted positions and widths of all peaks in Figure 1 is provided in SI.

Higher-resolution images of regions with diverging moiré periodicity are shown in Figure 2. We find that the bright topographic features (Figure 2a), which have a characteristic separation of 100−200 nm, run along one of three specific directions with a relative orientation of 120° and that their width is highly uniform. An image with lattice resolution (Figure 2c) of the area highlighted in Figure 2a, where one of the F−K domain walls terminates, shows that these lines are oriented at 30° to the lattice vectors of graphene (these directions are overlaid on Figure 2c). Profiles (Figure 2b) along the paths identified in Figure 2a,c show an apparent height of ~40 ± 4 pm and FWHM of 21 ± 2 nm as measured in AC mode, while in contact mode the apparent height is ~64 ± 4 pm and the FWHM is 6 ± 0.5 nm. Note that the difference in apparent dimension arises from the different imaging modality

employed which tracks contours of constant amplitude of a driven cantilever (AC mode) or constant deflection (contact mode). Both values of effective width are greater than that observed by Woods et al.[6] who use peak force tapping mode that provides a measure of the variation in local Youngs modulus.

A schematic cross-section of an F−K domain wall is shown in Figure 2g; here the periodic potential minima due to the hBN are represented by the red sinusoid, while the filled black circles correspond to carbon atoms. At the edges of the schematic, the carbon atoms sit in their preferred positions above the potential minima arising from the hBN substrate, but at the center there is an extra row of carbon atoms (viewed in cross-section). Thus, the lattice constant varies across the graphene and is larger at the center of the moiré cell than at the edge.[6]

If the assignment to F−K domain walls is correct, we expect that the bright topographic lines can only terminate at the origin of an edge dislocation in the graphene lattice. This is confirmed by a high-resolution AFM image (Figure 2d) in which a hexagonal closed path with edges corresponding to 17 lattice constants is overlaid on the image; we find that the start and end points of the circuit do not coincide (these are marked by the yellow and red points on the circuit). The difference between these points corresponds to the Burgers vector for a defect enclosed by the path; this has a magnitude equal to one lattice constant and is oriented normal to the bright topographic lines and, therefore, parallel to one of the graphene
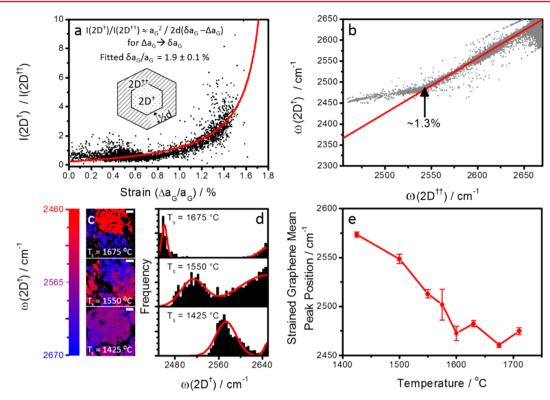
Figure 3. Raman analysis of the transition to lattice-matching. (a) The ratio of the intensities of the two 2D Raman bands as a function of strain (estimated from the Raman peak position (see Figure S2 and discussion in SI). The red line shows a fit of the data to a model based on our assignment of the two bands to the center ($2D^{\dagger}$) and edge regions ($2D^{\dagger\dagger}$) of the moiré pattern (inset and SI). (b) The position of the two 2D bands plotted against each other from samples grown at temperatures ranging from 1425 to 1710 °C. The red line shows the trend for strains up to 1.3%. (c,d) Statistical analysis of peak fitted Raman spectral maps for the $2D^{\dagger}$ band. (c) False color maps of $\omega(2D^{\dagger})$, scale bar: 5 μm, while (d) shows frequency distribution histograms of the same data. The red line shows a bi-Gaussian fit. The effect of temperature on the position of the most red-shifted Gaussian domain (indicative of strained graphene) is shown in (e). Additional data for other growth temperatures as well as equivalent plots for the $2D^{\dagger\dagger}$ band are included in SI.

lattice vectors. This observation provides direct confirmation that a commensurate−incommensurate transition[6] occurs and that the sources of network lines correspond to the introduction of an additional row of carbon atoms. The central regions of graphene in Figure 2a,e are thus lattice-matched to hBN with strain relief in the neighboring regions provided by point-like defects which act as the source for additional rows of carbon atoms leading to progressively smaller moiré periods.

At low red-shift, the $2D^{\dagger\dagger}$ peak has a higher intensity than the $2D^{\dagger}$ peak (see Figure 1 and additional spectra in SI), but is weaker for higher red-shift. We have previously suggested[19] that the $2D^{\dagger}$ and $2D^{\dagger\dagger}$ bands could arise from, respectively, the center of the moiré cell where the strain is isotropic,[16,29] and the edges where it is uniaxial. The relative intensity of the two Raman bands might therefore be expected to be proportional to the ratio of the effective areas of the central ($2D^{\dagger}$) and edge ($2D^{\dagger\dagger}$) regions of the moiré unit cell. In Figure 3, we compare the measured dependence on strain of the intensity ratio, $I(2D^{\dagger})/I((2D^{\dagger\dagger})$ with a simple model which assumes that the edge region has a fixed width, d, independent of the strain. In the limit $\lambda_S \gg d$, this leads to the following form, $I(2D^{\dagger})/I((2D^{\dagger\dagger}) \approx a_G^2/2d(\delta a_G - \Delta a_G)$ where $\delta a_G = (a_{hBN} - a_G)$, the mismatch between the lattice constants of unstrained hBN and graphene. The intensity ratio is expected to diverge as the strain approaches the lattice-matching condition. This is consistent with our observations and a fit to the data in Figure 3 gives a value of $1.9 \pm 0.1\%$ for $\delta a_G/a_G$, close to the expected value, 1.8% (see Figure S2 and associated discussion in SI for more

details of the fitting procedure including the determination of the strain from Raman data). Note that for lattice-matching the fraction of material at the edge regions is negligibly small and the associated $2D^{\dagger\dagger}$ peak is no longer present, as observed in Figure 1a. We also assign the $G^{\dagger}$ and $G^{\dagger\dagger}$ features to the two different graphene environments (center and edge of the moiré cell respectively; see SI).

An interesting critical behavior is revealed in Figure 3b, which shows a scatter plot of the Raman shifts, $\omega(2D^{\dagger})$ and $\omega(2D^{\dagger\dagger})$. For strains up to ~1.3%, which corresponds to $\lambda_S = 50$ nm, we observe a linear dependence (red line), followed by an abrupt change in gradient for higher strains. We suggest that this change occurs when the average strain is sufficiently high for the graphene at the center of the moiré cell to be lattice-matched with the hBN substrate. This would imply that the strain at the center of the moiré cell is close to 1.8% when the average strain is 1.3%, while the strain at the edges is <1.3%. Further increases of the average strain beyond this value results in an increase of the fraction of the moiré cell area which is lattice-matched, but the maximum strain and therefore the $2D^{\dagger}$ Raman shift will remain approximately constant. In contrast, the strain at the edges and the red-shift of the $2D^{\dagger\dagger}$ Raman peak will continue to increase until the average strain is ~1.8% at which point the moiré period diverges, the edge regions effectively disappear, and the $2D^{\dagger\dagger}$ peak loses intensity and merges with the $2D^{\dagger}$ peak.

We have extracted the dependence of the strain on the growth temperature from Raman maps of the sample, as shown
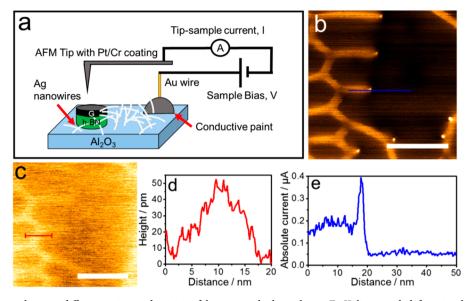
Figure 4. cAFM images showing differences in conductivity of lattice-matched graphene, F−K lines, and defects in the graphene lattice. (a) Experimental setup used for measuring the graphene electrical properties. The hBN/graphene heterostructure is grown on a sapphire (Al_2O_3) substrate and followed by Ag nanowire deposition. This provides a conducting pathway across the insulating Al_2O_3 surface to an electrical contact allowing the application of a sample bias and cAFM measurements to be recorded using a Pt/Cr coated tip (see SI for more information). (b) cAFM image recorded with a sample bias of −50 mV showing high current flow above F−K domain walls and very high current at bright pointlike features due to defects in the graphene lattice. (c) Contact mode AFM height trace image recorded simultaneously with (b). The scale bar is 50 nm in (b,c). The colormap contrast ranges from −0.03 to −0.41 µA in (b) and spans a range of 280 pm in (c). (d) Height profile averaged along the line with a width of 20 pixels indicated in (c). (e) A current profile measured along the line shown in (b). The current measured at the termination points is ∼2.5 times the value recorded at the F−K lines, when measured relative to the current within the intermediate regions.

in Figure 3. Raman spectra were acquired at each point (in a square map of dimensions 32×32 µm^2) and the band position, $\omega(2D^\dagger)$, was extracted using a fitting procedure (see SI) for samples grown at temperatures between 1425 and 1710 °C. For selected growth temperatures in Figure 3, spatial maps of $\omega(2D^\dagger)$ show regions of highly strained material (red) coexisting with regions (blue) where the strain is much lower. From our AFM scans, we believe that the bluer regions correspond to areas of graphene which were initially strained but relaxed postgrowth through the propagation of cracks.[19] For each temperature we also show a histogram of the number of pixels with a given value of $\omega(2D^\dagger)$ revealing a bi-Gaussian distribution corresponding to strained and relaxed graphene. The extracted mean peak position of the strained material confirms a systematic increase in the Raman shift (and strain) with growth temperature up to ∼1600 °C (see Figure 3e). Above this temperature, $\omega(2D^\dagger)$ is approximately constant (about 2460−2480 cm^{-1}) indicative of lattice-matched graphene at the center of the moiré cell. Further maps and histograms for additional temperatures and the dependence of the 2D†† peak are included in SI.

The electrical properties of the MBE-grown graphene layers have been investigated using conductive AFM (cAFM) which allows simultaneous contact mode AFM and measurements of local conductance. Samples are prepared, as shown in Figure 4a, by depositing an overlay of Ag nanowires to provide an electrical connection from the graphene across the insulating sapphire substrate to a counter electrode. The nanowires are deposited from solution and have a typical resistance of 200−400 Ω/square. Their use avoids the requirement for lithographically defined contacts which can lead to surface contamination through the application of polymeric resists (see SI for more details and further results from devices which

are fabricated after mechanical transfer of graphene/hBN flakes to a Si/SiO$_2$ substrate).

In the conductive AFM mode of imaging, the probe is scanned in contact mode, that is, a feedback loop is used to regulate the height of the cantilever so that the force between the tip and sample and, thus to first order, the tip−sample separation is constant along the trajectory of the tip. A fixed voltage is applied to the sample and the current at each point is measured. Images of the current variation for a region of highly strained graphene (Figure 4b; sample bias −50 mV) show that the current flow is significantly greater when the probe is above the F−K domain walls as compared with the neighboring lattice-matched regions and even higher where the walls terminate at defects in the graphene lattice (the bright pointlike features in Figure 4b). Note that the network of domain walls is also resolved in topographic contact mode images which are acquired simultaneously (Figure 4c).

A current profile extracted from this region shows an increase in current by a factor ∼3 above a domain wall (Figure 4e). A topographic height profile extracted from contact mode image (Figure 4d) shows that the cantilever probe is withdrawn by 47 ± 5 pm as it passes over the domain wall; this is close to the effective heights determined in Figure 2b and provides evidence that the probe-sample separation is approximately constant during the electrical measurements (additional data showing the current variation from this region acquired with the scan rotated through 90° is included in the SI and confirms that the current increase is not due to scanning artifacts related to feedback and/or hysteresis effects). The increase in current must therefore be due to a variation in the intrinsic electronic properties of graphene in the nanoscale regions close to the domain walls.

A higher current flow from the AFM probe to the surface when it is positioned above a F−K domain wall may be due to a

higher density of states in these regions. The value of the energy gap which is formed in lattice-matched graphene/hBN has been predicted[14] to be ~50 meV, close to $2k_BT$ at room temperature. The lower currents measured above the lattice-matched regions are consistent with a lower density of states which might be expected in the presence of a band gap which is of order a few times k_BT. Interestingly, the lattice-matching is absent in the graphene folds which form the F–K domain walls (see Figure 2g) and the band gap in these regions would be expected to be smaller or completely absent. Although there has been no detailed study of the quantum properties of F–K domain walls embedded in lattice-matched graphene, the one-dimensional symmetry is likely to promote analogies with conduction in carbon nanotubes.

We also observe enhanced current flow close to the topological defects which terminate the F–K lines; here the difference in conductance is much greater, six times, than over the lattice-matched regions. From a chemical perspective, there is at least one carbon atom which is not bonded to three neighboring carbon atoms at these defect sites and it is possible that these unsatisfied bonds lead to a higher local density of states. We highlight an analogy between the enhanced current above the defects in Figure 4 with the formation of edge contacts to graphene embedded between hBN sheets;[40] in both cases low resistance contacts are formed to a region of graphene where the carbon lattice has been disrupted.

Our Raman and AFM results provide conclusive evidence that it is possible to grow domains of lattice-matched graphene on hBN using high-temperature MBE. This lattice-matched region evolves laterally into graphene with reduced strain through the introduction of defects and associated domain walls (Figure 2e). Figure 2f shows a larger area scan in which isolated islands of turbostratic graphene are also observed (such regions give rise to the aggregate peaks in the Raman spectrum); in addition there are rows of these aggregates along step edges and/or cracks in the hBN substrate. This larger scale morphology is typical of the regions where we find the lattice-matched material, and as we have suggested previously[19] it is possible that these aggregates provide pinning sites which maintain the strain in the epitaxial graphene when cooling down from the high growth temperatures employed in this growth process.

Our results demonstrate an enhanced conductance of F–K defects embedded in highly strained graphene with the topological defects at their termination providing contact points of lower resistance. In this regime, the graphene might therefore be considered as a network of conducting quantum pathways rather than a homogeneous conductor. We believe that the novel material that can be grown using high-temperature MBE shows great promise both in realizing the long-standing objective of the introduction of a bandgap into graphene and the exploration of one-dimensional conductors and their junctions.

■ ASSOCIATED CONTENT

Ⓢ Supporting Information

The Supporting Information is available free of charge on the ACS Publications website at DOI: 10.1021/acs.nano-lett.7b04453.

> Experimental and growth methodologies; discussion of assignment of Raman peaks; conductive AFM sample preparation and protocols (PDF)

■ AUTHOR INFORMATION

Corresponding Author

*E-mail: peter.beton@nottingham.ac.uk.

ORCID Ⓞ

James C. Thomas: 0000-0003-3413-6427
Andrei N. Khlobystov: 0000-0001-7738-4098
Kenji Watanabe: 0000-0003-3701-8119
Peter H. Beton: 0000-0002-2120-8033

Notes

The authors declare no competing financial interest.
The original data on which this paper is based may be publicly accessed at https://rdmc.nottingham.ac.uk/ under doi.org/10.17639/nott.336.

■ REFERENCES

(1) Dean, C. R.; Young, A. F.; Meric, I.; Lee, C.; Wang, L.; Sorgenfrei, S.; Watanabe, K.; Taniguchi, T.; Kim, P.; Shepard, K. L.; Hone, J. *Nat. Nanotechnol.* 2010, 5, 722−726.
(2) Geim, A. K.; Grigorieva, I. V. *Nature* 2013, 499, 419−425.
(3) Wallbank, J. R.; Mucha-Kruczyński, M.; Chen, X.; Fal'ko, V. I. *Ann. Phys.* 2015, 527, 359−376.
(4) Hunt, B.; Sanchez-Yamagishi, J. D.; Young, A. F.; Yankowitz, M.; LeRoy, B. J.; Watanabe, K.; Taniguchi, T.; Moon, P.; Koshino, M.; Jarillo-Herrero, P.; Ashoori, R. C. *Science* 2013, 340, 1427−1430.
(5) Ponomarenko, L. A.; Gorbachev, R. V.; Yu, G. L.; Elias, D. C.; Jalil, R.; Patel, A. A.; Mishchenko, A.; Mayorov, A. S.; Woods, C. R.; Wallbank, J. R.; Mucha-Kruczynski, M.; Piot, B. A.; Potemski, M.; Grigorieva, I. V.; Novoselov, K. S.; Guinea, F.; Fal'ko, V. I.; Geim, A. K. *Nature* 2013, 497, 594−597.
(6) Woods, C. R.; Britnell, L.; Eckmann, A.; Ma, R. S.; Lu, J. C.; Guo, H. M.; Lin, X.; Yu, G. L.; Cao, Y.; Gorbachev, R. V.; Kretinin, A. V.; Park, J.; Ponomarenko, L. A.; Katsnelson, M. I.; Gornostyrev, Y. N.; Watanabe, K.; Taniguchi, T.; Casiraghi, C.; Gao, H.; Geim, A. K.; Novoselov, K. S. *Nat. Phys.* 2014, 10, 451−456.
(7) Yankowitz, M.; Xue, J.; Cormode, D.; Sanchez-Yamagishi, J. D.; Watanabe, K.; Taniguchi, T.; Jarillo-Herrero, P.; Jacquod, P.; LeRoy, B. J. *Nat. Phys.* 2012, 8, 382−386.
(8) Dean, C. R.; Wang, L.; Maher, P.; Forsythe, C.; Ghahari, F.; Gao, Y.; Katoch, J.; Ishigami, M.; Moon, P.; Koshino, M.; Taniguchi, T.; Watanabe, K.; Shepard, K. L.; Hone, J.; Kim, P. *Nature* 2013, 497, 598−602.
(9) Yankowitz, M.; Watanabe, K.; Taniguchi, T.; San-Jose, P.; LeRoy, B. J. *Nat. Commun.* 2016, 7, 13168.
(10) Xue, J.; Sanchez-Yamagishi, J.; Bulmash, D.; Jacquod, P.; Deshpande, A.; Watanabe, K.; Taniguchi, T.; Jarillo-Herrero, P.; LeRoy, B. J. *Nat. Mater.* 2011, 10, 282−285.
(11) Decker, R.; Wang, Y.; Brar, V. W.; Regan, W.; Tsai, H.; Wu, Q.; Gannett, W.; Zettl, A.; Crommie, M. F. *Nano Lett.* 2011, 11, 2291−2295.
(12) Sachs, B.; Wehling, T. O.; Katsnelson, M. I.; Lichtenstein, A. I. *Phys. Rev. B* 2011, 84, 195414.
(13) Kindermann, M.; Uchoa, B.; Miller, D. L. *Phys. Rev. B* 2012, 86, 115415.

(14) Giovannetti, G.; Khomyakov, P. A.; Brocks, G.; Kelly, P. J.; van den Brink, J. *Phys. Rev. B* **2007**, *76*, 73103.

(15) Jung, J.; DaSilva, A. M.; MacDonald, A. H.; Adam, S. *Nat. Commun.* **2015**, *6*, 6308.

(16) San-Jose, P.; Gutiérrez-Rubio, A.; Sturla, M.; Guinea, F. *Phys. Rev. B* **2014**, *90*, 75428.

(17) Neek-Amal, M.; Peeters, F. M. *Appl. Phys. Lett.* **2014**, *104*, 173106.

(18) Chen, Z.-G.; Shi, Z.; Yang, W.; Lu, X.; Lai, Y.; Yan, H.; Wang, F.; Zhang, G.; Li, Z. *Nat. Commun.* **2014**, *5*, 4461.

(19) Summerfield, A.; Davies, A.; Cheng, T. S.; Korolkov, V. V.; Cho, Y.; Mellor, C. J.; Foxon, C. T.; Khlobystov, A. N.; Watanabe, K.; Taniguchi, T.; Eaves, L.; Novikov, S. V.; Beton, P. H. *Sci. Rep.* **2016**, *6*, 22440.

(20) Tang, S.; Wang, H.; Zhang, Y.; Li, A.; Xie, H.; Liu, X.; Liu, L.; Li, T.; Huang, F.; Xie, X.; Jiang, M. *Sci. Rep.* **2013**, *3*, 2666.

(21) Yang, W.; Chen, G.; Shi, Z.; Liu, C.-C.; Zhang, L.; Xie, G.; Cheng, M.; Wang, D.; Yang, R.; Shi, D.; Watanabe, K.; Taniguchi, T.; Yao, Y.; Zhang, Y.; Zhang, G. *Nat. Mater.* **2013**, *12*, 792−797.

(22) Wofford, J. M.; Nakhaie, S.; Krause, T.; Liu, X.; Ramsteiner, M.; Hanke, M.; Riechert, H.; Lopes, J. M. J. *Sci. Rep.* **2017**, *7*, 43644.

(23) Dabrowski, J.; Lippert, G.; Schroeder, T.; Lupina, G. *Appl. Phys. Lett.* **2014**, *105*, 191610.

(24) Garcia, J. M.; Wurstbauer, U.; Levy, A.; Pfeiffer, L. N.; Pinczuk, A.; Plaut, A. S.; Wang, L.; Dean, C. R.; Buizza, R.; Van Der Zande, A. M.; Hone, J.; Watanabe, K.; Taniguchi, T. *Solid State Commun.* **2012**, *152*, 975−978.

(25) Zuo, Z.; Xu, Z.; Zheng, R.; Khanaki, A.; Zheng, J.-G.; Liu, J. *Sci. Rep.* **2015**, *5*, 14760.

(26) Lin, M.-Y.; Guo, W.-C.; Wu, M.-H.; Wang, P.-Y.; Liu, T.-H.; Pao, C.-W.; Chang, C.-C.; Lee, S.-C.; Lin, S.-Y. *Appl. Phys. Lett.* **2012**, *101*, 221911.

(27) Tang, S.; Wang, H.; Wang, H. S.; Sun, Q.; Zhang, X.; Cong, C.; Xie, H.; Liu, X.; Zhou, X.; Huang, F.; Chen, X.; Yu, T.; Ding, F.; Xie, X.; Jiang, M. *Nat. Commun.* **2015**, *6*, 6499.

(28) Chen, L.; He, L.; Wang, H. S.; Wang, H.; Tang, S.; Cong, C.; Xie, H.; Li, L.; Xia, H.; Li, T.; Wu, T.; Zhang, D.; Deng, L.; Yu, T.; Xie, X.; Jiang, M. *Nat. Commun.* **2017**, *8*, 14703.

(29) Argentero, G.; Mittelberger, A.; Reza Ahmadpour Monazam, M.; Cao, Y.; Pennycook, T. J.; Mangler, C.; Kramberger, C.; Kotakoski, J.; Geim, A. K.; Meyer, J. C. *Nano Lett.* **2017**, *17*, 1409−1416.

(30) Cheng, T. S.; Davies, A.; Summerfield, A.; Cho, Y.; Cebula, I.; Hill, R. J. A.; Mellor, C. J.; Khlobystov, A. N.; Taniguchi, T.; Watanabe, K.; Beton, P. H.; Foxon, C. T.; Eaves, L.; Novikov, S. V. *J. Vac. Sci. Technol., B.* **2016**, *34*, 02L101.

(31) Albar, J. D.; Summerfield, A.; Cheng, T. S.; Davies, A.; Smith, E. F.; Khlobystov, A. N.; Mellor, C. J.; Taniguchi, T.; Watanabe, K.; Foxon, C. T.; Eaves, L.; Beton, P. H.; Novikov, S. V. *Sci. Rep.* **2017**, *7*, 6598.

(32) Mohiuddin, T. M. G.; Lombardo, A.; Nair, R. R.; Bonetti, A.; Savini, G.; Jalil, R.; Bonini, N.; Basko, D. M.; Galiotis, C.; Marzari, N.; Novoselov, K. S.; Geim, A. K.; Ferrari, A. C. *Phys. Rev. B* **2009**, *79*, 205433.

(33) Tsoukleri, G.; Parthenios, J.; Papagelis, K.; Jalil, R.; Ferrari, A. C.; Geim, A. K.; Novoselov, K. S.; Galiotis, C. *Small* **2009**, *5*, 2397−2402.

(34) Ferrari, A. C.; Meyer, J. C.; Scardaci, V.; Casiraghi, C.; Lazzeri, M.; Mauri, F.; Piscanec, S.; Jiang, D.; Novoselov, K. S.; Roth, S.; Geim, A. K. *Phys. Rev. Lett.* **2006**, *97*, 187401.

(35) Shin, Y.; Lozada-Hidalgo, M.; Sambricio, J. L.; Grigorieva, I. V.; Geim, A. K.; Casiraghi, C. *Appl. Phys. Lett.* **2016**, *108*, 221907.

(36) Zabel, J.; Nair, R. R.; Ott, A.; Georgiou, T.; Geim, A. K.; Novoselov, K. S.; Casiraghi, C. *Nano Lett.* **2012**, *12*, 617−621.

(37) Reich, S.; Ferrari, A. C.; Arenal, R.; Loiseau, A.; Bello, I.; Robertson, J. *Phys. Rev. B* **2005**, *71*, 205201.

(38) Cançado, L. G.; Jorio, A.; Ferreira, E. H. M.; Stavale, F.; Achete, C. A.; Capaz, R. B.; Moutinho, M. V. O.; Lombardo, A.; Kulmala, T. S.; Ferrari, A. C. *Nano Lett.* **2011**, *11*, 3190−3196.

(39) Malard, L. M.; Pimenta, M. A.; Dresselhaus, G.; Dresselhaus, M. S. *Phys. Rep.* **2009**, *473*, 51−87.

(40) Wang, L.; Meric, I.; Huang, P. Y.; Gao, Q.; Gao, Y.; Tran, H.; Taniguchi, T.; Watanabe, K.; Campos, L. M.; Muller, D. A.; Guo, J.; Kim, P.; Hone, J.; Shepard, K. L.; Dean, C. R. *Science* **2013**, *342*, 614−617.